

GRB 241030A: a prompt thermal X-ray emission component and diverse origin of the very early UVOT WHITE and U band emission

QIU-LI WANG ^{1,2} HAO ZHOU ¹ YUN WANG ¹ JIA REN ¹ SAMAPORN TINYANONT ³ DONG XU ⁴
NING-CHEN SUN,^{5,4,6} JOHAN P.U. FYNBO ^{7,8} DANIELE B. MALESANI ^{7,8} JIE AN,^{4,5} RUNGRIT ANUTARAWIRAMKUL,³
PATHOMPONG BUTPA,³ SHAO-YU FU,⁴ SHUAI-QING JIANG,^{4,5} XING LIU,^{4,5} KRITSADA PALEE,³ PAKAWAT PRASIT,³
ZI-PEI ZHU ⁴ ZHI-PING JIN ^{1,2} AND DA-MING WEI ^{1,2}

¹Key Laboratory of Dark Matter and Space Astronomy, Purple Mountain Observatory, Chinese Academy of Sciences, Nanjing 210023, China

²School of Astronomy and Space Science, University of Science and Technology of China, Hefei 230026, China

³National Astronomical Research Institute of Thailand, 260 Moo 4, Donkaew, Maerim, Chiang Mai 50180, Thailand

⁴National Astronomical Observatories, Chinese Academy of Sciences, Beijing 100049, China

⁵School of Astronomy and Space Science, University of Chinese Academy of Sciences, Beijing 100049, China

⁶Institute for Frontiers in Astronomy and Astrophysics, Beijing Normal University, Beijing 102206, China

⁷Cosmic Dawn Center (DAWN), Copenhagen 2200, Denmark.

⁸Niels Bohr Institute, Copenhagen University, Jagtvej 155, DK-2200, Copenhagen N, Denmark

ABSTRACT

We present a detailed analysis of the long-duration GRB 241030A detected by *Swift*. Thanks to the rapid response of XRT and UVOT, the strongest part of the prompt emission of GRB 241030A has been well measured simultaneously from optical to hard X-ray band. The time-resolved WHITE band emission shows strong variability, largely tracing the activity of the prompt gamma-ray emission, may be produced by internal shocks too. The joint analysis of the XRT and BAT data reveals the presence of a thermal component with a temperature of a few keV, which can be interpreted as the photosphere radiation, and the upper limit of the Lorentz factor of this region is found to range between approximately 20 and 80. The time-resolved analysis of the initial U-band exposure data yields a very rapid rise ($\sim t^{5.3}$) with a bright peak reaching 13.6 AB magnitude around 410 seconds, which is most likely attributed to the onset of the external shock emission. The richness and fineness of early observational data have made this burst a unique sample for studying the various radiation mechanisms of gamma-ray bursts.

Keywords: Gamma-ray bursts (629)

1. INTRODUCTION

Gamma-ray bursts (GRBs) are the most powerful explosions in the universe. Several models like dissipative photosphere, internal shock and magnetic dissipation have been developed to explain the nature of prompt emission, and the afterglow emission is thought to originate from the external shock composed of a forward shock (FS) and a reverse shock (RS), which were only detected in some GRBs (Mészáros & Rees 1997, 1999; Sari & Piran 1999).

Only a few optical observations have been made contemporaneous with gamma-ray bursts, due to the limitation of the response speed of optical instruments in the past. The first optical flash discovered in the prompt phase is GRB 990123 (Akerlof et al. 1999). Its bright emission in the optical band can be explained by the reverse shock of a thin shell (Fan et al. 2002; Zhang et al. 2003). The rapid response and precise localization capabilities of the *Swift* mission (Gehrels et al. 2004) make it possible to obtain simultaneous data from the optical band to the γ -ray band. Furthermore, Space-based multi-band astronomical Variable Objects Monitor (SVOM), with four onboard instruments

launched in 2024, has a larger field-of-view (FOV) and higher sensitivity which enhances the possibility to observe GRB from the optical band to the γ -ray band at an early stage (Godet et al. 2014; Wei & Cordier 2024; Wang et al. 2024). Several models have been developed to explain bright optical flashes of GRBs at the early stage. For example, the early-time optical emission could be the onset of the afterglow emission (either from FS or RS), and some argue early optical flashes of GRBs can usually arise from the internal shock (Wei 2007). Some physical properties of GRB ejecta can be constrained from very early afterglow emission data, e.g., the magnetized degree of the outflow powering GRBs (Fan et al. 2004; Zhang & Kobayashi 2005). Hence, a systematic study of multi-band emission of GRBs at the early stage is helpful to constrain GRB emission models.

In this article, we report the analysis of long GRB 241030A data obtained by the Neil Gehrels *Swift*. The *Swift* burst alert telescope (BAT, Barthelmy et al. 2005) was triggered by a precursor of GRB 241030A at 100 seconds before the main burst, leading to *Swift* performed multi-band observations of the prompt phase with high temporal resolution, using the X-ray telescope (XRT, Burrows et al. 2005) and the ultraviolet/optical telescope (UVOT, Roming et al. 2005). Similar to Jin et al. (2023) and Zhou et al. (2023), we split the UVOT data taken in the event mode to short time bins to explore the optical temporal behavior at the early stage of the burst. The prompt γ -ray emission of this burst exhibits several pulses overlapped with each other. Similar temporal behavior is also seen in the optical and X-ray data. After the prompt phase, the U-band data shows a bump peaking around 410s after the trigger, which is attributed as the onset of the afterglow. The early behavior of the afterglow is well sampled, which sets good constraints for parameters of the standard fireball model.

We carried out ground-based optical follow-up using the Thai Robotic Telescope (TRT) and the Nordic Optical Telescope (NOT), observations and the reduction of the data are described in Sec 2. The prompt emission analysis and board-band spectral fit results are presented in Sec 3, and the afterglow analysis are presented in Sec 4. In Sec 5, we summarize and discuss our work. The standard cosmology model with $H_0 = 67.4 \text{ km s}^{-1}\text{Mpc}^{-1}$, $\Omega_M = 0.315$ and $\Omega_\Lambda = 0.685$ (Planck Collaboration et al. 2020) is adopted in this paper. All errors are given at the 1σ confidence level unless otherwise stated.

2. OBSERVATIONS AND DATA REDUCTIONS

2.1. Observations

At 05:48:03 UT on October 30, 2024 (T_0), GRB 241030a simultaneously triggered Fermi-GBM and *Swift*/BAT (Fermi GBM Team 2024; Klingler et al. 2024). Based on the BAT localization, *Swift* immediately slewed to the source and initiated follow-up observations. Then a bright, uncatalogued X-ray source was identified by XRT 73.5 s after BAT trigger at the location RA = 22h 52m 33.30s, DEC = +80° 26' 59.6" (J2000) with a 90% uncertainty of 2.2" (Beardmore et al. 2024). UVOT began to observe the field of GRB 241030A about 83 seconds after the BAT trigger in the event mode (Breeveld et al. 2024). In addition, Fermi-LAT also detected GeV photons from this event (Pillera et al. 2024). Furthermore, SVOM/VT observed the field of GRB 241030A via ToO observations started at 07:03:11 UTC, about 1.25 hours after the burst (SVOM/VT commissioning Team et al. 2024). The VT conducted observations simultaneously in two channels: VT_B (400nm-650nm) and VT_R (650nm-1000nm). SVOM/C-GFT start to observe the field of GRB 241030A on 09:54:53 UT, about 4.09 hours after the trigger in the commissioning phase (SVOM/C-GFT Team et al. 2024). A series of g, r and i band images were obtained with exposure time of 30 seconds. The SVOM/GRM was triggered in-flight by GRB 241030A at 05:48:14 U (SVOM/GRM Team et al. 2024). However, at the time of the burst ECLAIRs was not collecting data. In addition, the optical counterpart of GRB 241030A was observed with the Low Resolution Imaging Spectrometer on the Keck I 10 m telescope, revealing a continuum spectrum and narrow absorption lines, with a likely redshift of 1.411 (Zheng et al. 2024).

Approximately 26 minutes after T_0 , we manually triggered the 70 cm telescopes at Sierra Remote Observatories in the USA, one of the nodes of the worldwide Thai Robotic Telescope (TRT), obtaining continuous and complete light curve with 60 s, 90 s, and 180 s frames in the R band that lasted until three hours after the trigger time. About three days later, we acquired further observations in the Sloan g, r, and z band using the Nordic Optical Telescope (NOT; 2.56 m at the Roque de los Muchachos observatory, La Palma, Spain) telescope.

2.2. Data reduction

2.2.1. *Swift* Data

The data from *Swift* BAT and UVOT, was reduced with the HEASoft 6.34. The BAT light curve (15 - 350 keV) from $T_0 - 60\text{s}$ to $T_0 + 242\text{s}$ was extracted with a time bin size of 1 s. The XRT data was reduced with the online

Swift/XRT data products generator¹(Evans et al. 2007; Evans et al. 2009). UVOT observed GRB 2410301A in the V, B, U, W1, M2, W2 and WHITE bands for several epochs. For data taken in the image mode, we started from the level 2 UVOT products and made photometry with the standard aperture. For the WHITE-band and U-band data taken in the event mode, a fixed time bin of 5 s (10 s) was applied to extract the light curve in the WHITE (U) band. The standard aperture is also adopted to make photometries of the event data. The UVOT photometries are listed in Table 1 .

As shown in the Figure 1, the BAT light curve showed a complex structure with many overlapped pulses that lasted for about 250s. Generally, precursors are broadly defined as fainter emissions followed by a quiescent period before the main emission of the GRB (Bukhari et al. 2022). There is a quiescent period from ~ 50 to ~ 80 s after the BAT trigger, which suggests the first group of the γ -ray pulses could be the precursor emission. Compared with the second group of γ -ray pulses starting from $\sim T_0 + 100$ s as well as the precursor, the intensity of the small pulse from $\sim T_0 + 80$ to $T_0 + 90$ s is weak and followed by a short quiescent period lasting for about 10s implying the small pulse also could be the precursor emission. Hence, we suggest that GRB 241030A is a burst triggered by its precursor emission, and the true start time of the main prompt emission is about $T_0 + 100$ s, which is similar to another *Swift*/BAT GRB 060124 in the literature (Romano et al. 2006). The X-ray light curve also shows about ten pulses which almost trace the γ -ray light curve. The light curve in the WHITE band shows 5 peaks and the brightest one is around 148s. Only 4 optical peaks coincide with γ -ray peaks. The optical peak around 180s does not coincide with any γ -ray peak but with a small X-ray peak. The similarity between the UV/optical, X-ray and γ -ray light curves suggests that in the prompt phase, the UV/optical, X-ray and γ -ray emission may have the same origin (e.g., activities of the central engine or the internal shock). The U-band light curve is smoother than the WHITE-band light curve and clearly shows a bump at ~ 410 s with a steep rise and a normal decay which may originate from external shock region.

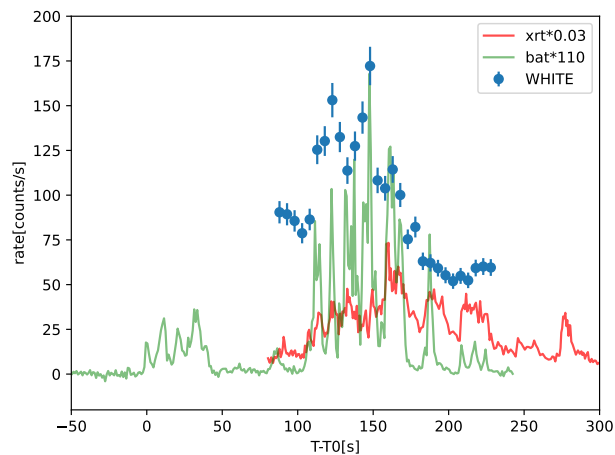


Figure 1. Multiband prompt emission light curves of GRB 241030A. Data are collected by *Swift* BAT (green), XRT (red), and UVOT (blue). Note that the UVOT data are all in WHITE band.

2.2.2. Fermi Data

Fermi-GBM is composed of 12 NaI(Tl) detectors and 2 BGO detectors (Meegan et al. 2009). Based on the angle between the source location and the pointing direction of each detector, and considering the poor quality of the BGO observation data, we selected only the n0 detector data for subsequent joint spectral analysis. And we used `GBM data tools` (Goldstein et al. 2022) to generate the files required for spectral analysis from the TTE (Time-Tagged Event) data.

In order to produce the GeV light curves, we also performed data reduction for the Fermi-LAT data. Fermi-LAT is a high-performance gamma-ray telescope designed for a photon energy range from 30 MeV to 1 TeV (Atwood et al.

¹ https://www.swift.ac.uk/burst_analyser/

2009). For the Fermi-LAT data reduction, we selected photon events within the energy range of 100 MeV to 100 GeV, using the TRANSIENT event class and the FRONT+BACK type. To minimize contamination from the Earth’s limb, photons with zenith angles exceeding 100° were excluded. Subsequently, we identified good time intervals by applying the quality filter condition (`(DATA_QUAL>0 && LAT_CONFIG==1)`). In the standard unbinned likelihood analysis procedure², we selected a 10° region centered on the location of GRB 241030A as the region of interest (ROI). The initial model for the ROI region, generated by the `make4FGLxml.py` script³, includes the galactic diffuse emission template (`gll_iem_v07.fits`), the isotropic diffuse spectral model for the TRANSIENT data (`iso_P8R3_TRANSIENT020_V3_v1.txt`) and all the Fourth Fermi-LAT source catalog (`gll_psc_v35.fit`; Ballet et al. 2023) sources. We defined GRB 241030A as a point source in the model file, with the model set to `PowerLaw2`⁴. And an automatic rebinning algorithm was employed, ensuring at least 10 photons per bin and a $TS > 9$ to guarantee that the flux in each bin is significant.

2.2.3. Ground-base Photometry

After conducting standard data reduction with the Image Reduction and Analysis Facility (Tody 1986) and performing astrometric calibration using Astrometry.net (Lang et al. 2010), the apparent photometry was calibrated against the Pan-STARRS1 DR2 catalog (Flewelling et al. 2020). The Johnson-Cousins filters were calibrated using magnitudes that were transformed from the Sloan system.⁵ The photometric results without Galactic extinction correction are tabulated in Table 2.

3. PROMPT EMISSION ANALYSIS

3.1. Broadband light curves of the prompt emission

XRT and UVOT began to observe GRB 241030A at $T_0 + 73.5$ s and $T_0 + 83$ s, respectively. Both XRT and UVOT obtained well-sampled data during the prompt phase for about 150 s. Combining the γ -ray data observed by BAT (15.0 keV to 150 keV) and GBM data (8 keV to 900 keV), the entire prompt phase ($\sim T_0 + 75$ s to $\sim T_0 + 250$ s) is almost covered by multi-band observations, which makes it possible to study the temporal and spectral properties of the prompt emission in detail.

Figure 1 shows multi-band light curves in the prompt phase. BAT data shows two groups of several peaks from T_0 to $T_0 + 50$ s and $T_0 + 80$ s to $T_0 + 230$ s with a peak at $T_0 + 148$ s. We consider the first group of peaks in BAT data as the precursor emission, which triggered BAT, and the second group is the prompt emission. XRT data show overlapped peaks and the brightest one is at $T_0 + 160$ s. The UVOT WHITE-band light curve in the prompt phase is binned with a temporal size of 5 s, and shows three major peaks, which seems to be correlated with the BAT data. Optical data with high temporal resolution provides clear evolution of the optical emission in the prompt emission. The brightest optical peak occurs at $\sim T_0 + 148$ s when the brightest γ -ray peak occurs. The other 2 optical peaks occur at $\sim T_0 + 123$ s and $\sim T_0 + 163$ s when the γ -ray light curve also peaks. Generally speaking, optical data exhibit complicated variability and partially trace the gamma-ray data, implying that they share the same origin and are mainly produced by internal shocks.

3.2. Spectral analysis of the prompt emission

The joint spectral fitting, including XRT (0.3 - 10 keV), BAT (15 - 150 keV), GBM/NaI (8 - 900 keV) and optical data, was performed with XSPEC (version 12.14.1). We sliced the prompt emission epoch ($T_0 + 85$ s to $T_0 + 230$ s) into 29 time intervals with a time bin size of 5 s aligned with the optical observation intervals. Given the suboptimal signal-to-noise ratio (SNR) of less than 3 in the GBM data at certain epochs, the GBM data within specific time intervals (105 to 175 seconds, 185 to 195 seconds, and 215 to 220 seconds) was only adopted for spectral fitting analysis. We jointly fit board-band data with the χ^2 statistic, except GBM data, for which the `pgstat` (i.e., Poisson data with Gaussian background) statistic was used. Similar to (Wang et al. 2023), four models with Galactic absorption (`tbabs`) and host galaxy (`ztbabs`) absorption were used here for spectral fitting, including power-law (PL), cutoff power-law (CPL), power-law with blackbody (PL+BB) and cutoff power-law with blackbody (CPL+BB). The Galactic equivalent hydrogen column density N_H is fixed as $1.79 \times 10^{21} \text{ cm}^{-2}$ (Ambrosi et al. 2024) and the host galaxy equivalent hydrogen column density could be ignored according to the fitting result of late-time ($> T_0 + 4500$ s) averaged XRT spectrum.

² <https://fermi.gsfc.nasa.gov/ssc/data/analysis/scitools/>

³ <https://fermi.gsfc.nasa.gov/ssc/data/analysis/user/>

⁴ https://fermi.gsfc.nasa.gov/ssc/data/analysis/scitools/source_models.html

⁵ <https://live-sdss4org-dr12.pantheonsite.io/algorithms/sdssUBVRITransform/#Lupton>

For some spectral energy distributions (SEDs), the SNR for $E \gtrsim 100$ keV is low and the cut energy of the CPL model is poorly constrained. Hence, the PL model is adopted to fit the data instead of CPL.

As shown in Figure 2, the X-ray to γ -ray SEDs clearly show excesses around ~ 10 keV when fitted with a PL or CPL model, and the excesses can be fitted by a thermal component. Compared to models that employ only CPL or PL, our analysis reveals that models incorporating both CPL+BB or PL+BB have better fitting results. Models with BB exhibit lower values of the Bayesian Information Criterion (BIC) compared to those without. BIC is defined as follow:

$$BIC = -2 \ln L + k \ln N \quad (1)$$

where L is the maximized value of the likelihood function of the model, k is the number of free parameters, N is the number of data points. Table 3 shows detail parameters of spectral fit and differences of BIC, Δ_{BIC} , between models with BB and models without BB in different time intervals. Except for the epoch 140 - 145 s where $\Delta_{\text{BIC}} = 2.97$, $\Delta_{\text{BIC}} > 10$ in all other epochs supports the existence of an additional thermal component and the Δ_{BIC} exceeds 30 in 20 of 29 epochs which is strong evidence of an additional thermal component. For the case in 140 - 145 s, the flux of blackbody derived from the fitted blackbody parameters is very low, so it may be covered by CPL or PL component, which is also reasonable.

3.3. Parameters of the Photospheric Radiation

With the best fitted temperature kT_{BB} and the flux F_{BB} of the thermal component, we can estimate physical parameters of the fireball model, e.g., the Lorentz factor of photosphere using the method in Pe'er et al. (2007). The

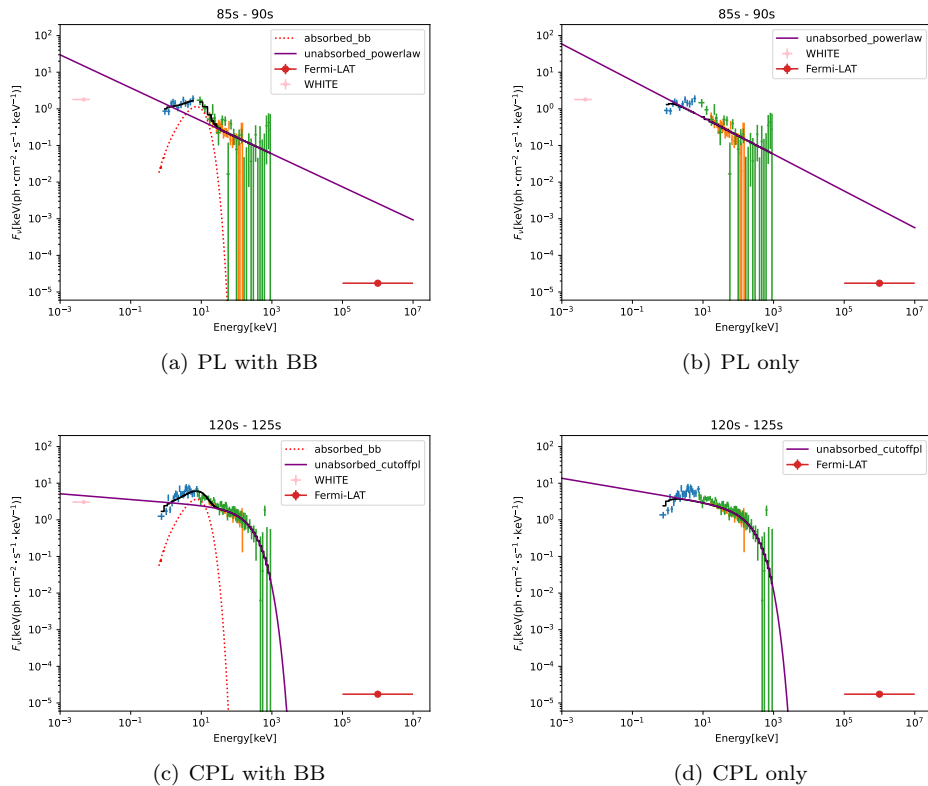


Figure 2. The SEDs of GRB 241030A prompt emission. (a) PL with BB: the spectral fitting of 85 s to 90 s interval in PL with BB model. (b) PL only: the spectral fitting of 85 s to 90 s interval in PL only model. (c) CPL with BB: the spectral fitting of 120 s to 125 s interval in CPL with BB model. (d) CPL only: the spectral fitting of 120 s to 125 s interval in CPL only model. Pink points represent observed optical flux density in WHITE band and red points represent Fermi-LAT data. Due to the low SNR of the Fermi-LAT data, here we used the average flux density over the 0-260 seconds within the energy range of 0.1-10 GeV. Dotted red lines represent absorbed BB component and purple solid lines represent unabsorbed PL or CPL component.

Lorentz factor of the photosphere Γ_{ph} is:

$$\Gamma_{\text{ph}} = \left[(1.06)(1+z)^2 d_L \frac{Y F^{ob} \sigma_T}{2m_p c^3 \mathcal{R}} \right]^{\frac{1}{4}} \quad (2)$$

where d_L is the luminosity distance, F^{ob} is the total observed flux of thermal and non-thermal components, m_p is the mass of the proton, σ_T is the Thomson scattering cross-section. In Pe'er's method, $Y = \epsilon/\epsilon_\gamma \geq 1$ is the ratio between the total fireball energy and the energy emitted in γ -ray. In our work, $Y = \epsilon/\epsilon_{\text{ob}}$ is the ratio between the total fireball energy and the observed energy emitted in 0.3 - 150 keV here we exhibit the upper limit of Γ_{ph} . \mathcal{R} is the ratio factor defined as:

$$\mathcal{R} \equiv \left(\frac{F_{BB}^{ob}}{\sigma T^{ob4}} \right)^{\frac{1}{2}} \quad (3)$$

where σ is Stefan-Boltzmann constant, T^{ob} and F_{BB}^{ob} are the observed temperature and flux of the thermal component. Combing Equation (2) and Equation (3), the Lorentz factor of photosphere Γ_{ph} can be calculated and the evolution of $\Gamma_{\text{ph}}/Y^{\frac{1}{4}}$ is shown in Figure 3.

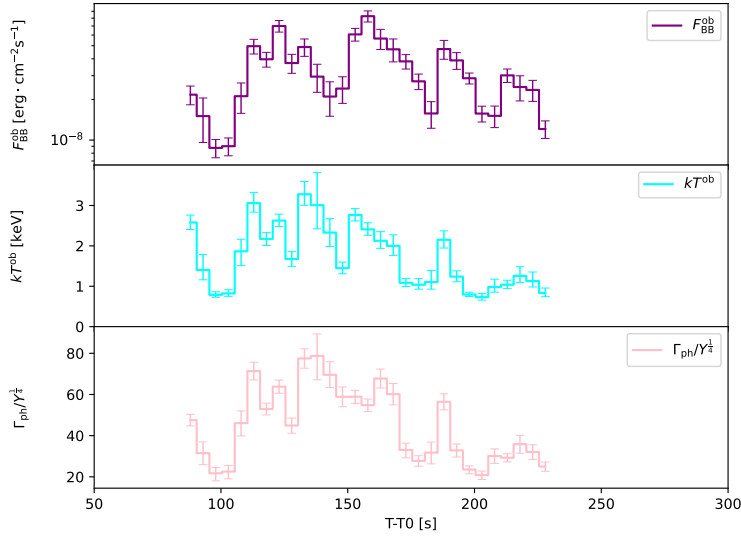


Figure 3. The evolution of different parameters for the thermal component in GRB 241030A. From top to bottom are the observed flux of the thermal component F_{BB}^{ob} , the observed temperature of the thermal component kT^{ob} and the Lorentz factor of the photosphere Γ_{ph} in the prompt emission, respectively.

4. AFTERGLOW EMISSION ANALYSIS

4.1. Temporal behavior of the afterglow

UV/optical light curves of the afterglow were phenomenologically fitted with a broken power-law (BPL) function, which has been widely used to fit afterglow light curves for both the rising and decay phases (e.g., Liang et al. 2007; Li et al. 2012; Wang et al. 2015; Huang et al. 2018). The best fitted BPL model of the afterglow light curve could provide an initial understanding of the physical properties of this burst. The BPL can be written as:

$$f(t) = A \left[\left(\frac{t}{t_b} \right)^{\alpha_1 \Delta} + \left(\frac{t}{t_b} \right)^{\alpha_2 \Delta} \right]^{-1/\Delta} \quad (4)$$

where A is the normalization factor, t_b is the break time, α_1 and α_2 are the temporal decay indices, Δ is the smooth parameter.

Since the γ -ray emission from T_0 to $T_0 + 100$ s could be the precursor emission, so the $T_0 + 100$ s is treated as the true start time of the burst (i.e., the launch time of the jet). The best fitted BPL model of UV/optical light curves gives $\alpha_1 = -5.3_{-0.3}^{+0.4}$ and $\alpha_2 = 1.3_{-0.1}^{+0.1}$. Note that α_2 is well constrained by 7 UVOT UV/optical bands. Hence, to account for the behavior of afterglow in the brightening phase, both RS and FS components should be considered, which is discussed in Section 4.3.

4.2. The spectral analysis of the afterglow

The epoch $T_0 + 755$ s is selected to construct the broad band SED since we have the best multi-band coverage data. To ensure a sufficient SNR, the XRT data from 706 to 806 s was collected to create the X-ray spectrum, with the equivalent photon arrival time of ~ 755 s. As shown above, all 7 UVOT UV/optical light curves in the decay phase can be well described by a power-law decay with a temporal decay index $\alpha_2 = 1.3_{-0.1}^{+0.1}$. Hence, the UV/optical data was interpolated to $T_0 + 755$ s. The interpolated UV/optical fluxes used to construct the broad band SED are listed in Table 4.

The broad band SED was fitted with an absorbed PL model $F_\nu \propto \nu^{-\beta}$. The Milky Way extinction model with $E(B - V) = 0.1148$ (Fitzpatrick 1999) and $R_V = 3.08$ is adopted. The N_H from photoionization absorption model is set to $1.79 \times 10^{21} \text{ cm}^{-2}$ (Wilms et al. 2000). For the host, the extinction model of Small Magellanic Cloud model is adopted. The best fitted result gives the spectral index $\beta = 1.12_{-0.01}^{+0.02}$ as predicted by the FS, the the $E(B - V)$ of the host galaxy is $0.19_{-0.01}^{+0.01}$, which is shown in Figure 4. During the Xspec fitting, the *tbabs* and *ztbabs* models are set as same as mentioned above. We tried both simple power-law and cut-off power-law model, however, we cannot use the cut-off power-law model here because the cutoff is in the γ -ray band and we don't have that detection at this epoch.

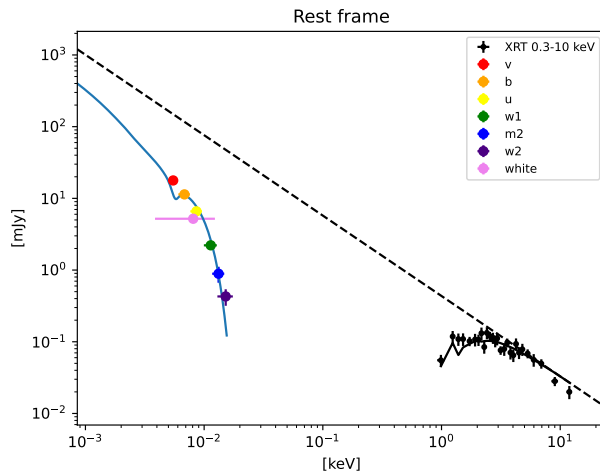


Figure 4. The broad band SED of GRB 241030A afterglow at 755 s after the BAT trigger. Black points are observed data of XRT from 0.3 keV to 10.0 keV. Colorful points are the observed data in different UV/optical bands. Blue and black solid line represent the predicted absorbed model. Dashed line is the unabsorbed power-law model with a spectral index of 1.12.

4.3. Afterglow modeling

After the prompt emission, the optical light curve is characterized by a steep rising to a peak around 410 s. The beginning of steep rise is not observed by the UVOT, but it can be constrained that the start time of the rising is after 228 s according to the last data in WHITE band. The peak reaches $U = 13.6$ AB mag, and following the peak, UV/optical light curves decay monotonically without significant color evolution.

Meanwhile, the X-ray data show a different temporal behavior. After the prompt emission, the X-ray light curve has several pulses from 230 s to 300 s and peaks around 278 s. After the peak, the X-ray light curve shows a monotonic decay with a temporal decay index of -1.2. After 10^5 s, a further steepening break in X-ray band is observed which is probably caused by a jet break.

The interaction between the relativistic outflow of the GRB and the circumburst medium induces the formation of a pair of relativistic shocks, i.e., FS and RS components. Initially the light curve is dominated by the RS emission

characterized by a steep rise and a rapid decay. The FS takes over soon after the U-band peak, and dominates the decay phase. The electrons accelerated by these shocks are capable of generating multi-band emissions via synchrotron radiation and inverse Compton scattering. Numerous computational paradigms for modeling afterglows have been developed, we use the Python-wrapped Fortran package (Ren et al. 2024) to perform numerical calculations of the radiation contributed from the FS component under the various effects. And the calculation of the contribution from the RS in the early afterglow is referenced from (Yi et al. 2013). Therefore, under this model, the flux density at a certain time and frequency is:

$$F_{t,\nu} = F(t, \nu, \Gamma_0, \epsilon_{e,f}, \epsilon_{B,f}, \theta_j, E_{k,\text{iso}}, p_f, \epsilon_{e,r}, \epsilon_{B,r}, p_r, n_0), \quad (5)$$

where Γ_0 is the initial Lorentz factor, ϵ_e is the fraction of the shock energy into the energy of relativistic electrons, ϵ_b is the fraction of the shock energy converted into the energy of magnetic field, θ_j is the half-opening angle of the jet in radians, $E_{k,\text{iso}}$ is the isotropic kinetic energy of the jet, p is the electron energy distribution index, n_0 is the number density of the circumburst medium. And the additional subscripts f and r represent the FS and RS, respectively.

We utilize PyMultiNest (Buchner et al. 2014) to conduct Bayesian inference on the parameters of the afterglow model (Eq. 5), setting the number of live points to 500. The prior ranges for these parameters are provided in Table 5. Additionally, we define a log-likelihood term for the each data point, which corresponds to an observation at time t_i in a band with central frequency ν_i , as follows:

$$\ln \mathcal{L}_i = -\frac{1}{2} \frac{(F_{t,\nu} - F_{t,\nu,\text{obs}})^2}{\sigma_i^2 + f_{\text{sys}}^2 F_{t,\nu,\text{obs}}^2} - \ln[2\pi(\sigma_i^2 + f_{\text{sys}}^2 F_{t,\nu,\text{obs}}^2)]. \quad (6)$$

where f_{sys} is a free parameter to characterize the systematic error. By fitting the light curves, we are able to constrain various parameters for both the FS and RS components. The best simultaneous fit results are shown in Figure 5 and parameters are summarized in Figure 6. According to the FS and RS models, we estimate that the initial Lorentz factor $\Gamma_0 \sim 135$, the half-opening angle $\theta_j \sim 5^\circ$. All the parameters are constrained well, except the the isotropic kinetic energy $E_{k,\text{iso}} \sim 10^{56}$ erg. The system error here is set as free to account for the bias of the central wavelength of the UVOT WHITE band, since the width of the WHITE band is so large that the reference value could be inaccurate. The fit also constrain well the fraction of the the forward shock energy converted into the energy of magnetic field $\epsilon_{B,f} = 2 \times 10^{-6}$ and the reverse shock energy converted into the energy of magnetic field $\epsilon_{B,r} = 7 \times 10^{-4}$, i.e., the reverse shock region is moderately magnetized, as found in GRB 990123 and other events (Fan et al. 2002; Zhang et al. 2003).

5. SUMMARY AND DISCUSSION

We presented a detailed analysis of the prompt emission and the early afterglow of GRB 241030A, and suggest GRB 241030A is a burst triggered by its precursor emission about 100s before the prompt emission. The prompt UV/optical light curve has several bumps, which roughly traces the prompt γ -ray emission. Shortly after the prompt emission, the optical light curve rises steeply and reaches a bright peak of U = 13.6 AB mag around 410 s, which is attributed to the RS emission of the afterglow. At the same time, the X-ray keeps decaying except for a flare around 278s. After 410s, both the UV/optical and X-ray light curves show normal decay behaviors. In this work, our main results are as follows:

(i) Because GRB 241030A was triggered by its precursor emission, *Swift*-XRT/UVOT were able to observe the prompt emission at a high temporal resolution. According to simultaneous multi-band observations, we find that emissions from UV/optical to γ -ray show similar complicated overlapped pulses, which suggests their may share the same origin. After the prompt phase, a U-band bump at ~ 410 s with a steep rising was observed, which is attributed to the onset of the afterglow. The comprehensive data of GRB 241030A in the prompt phase and the early afterglow phase makes it possible to study the mechanisms of emission and to constrain several parameters of the standard afterglow model.

(ii) In the prompt emission phase, the *Swift*/XRT, *Swift*/BAT and Fermi-GBM data were jointly fitted. We found that a thermal component is required to account for the excess in the X-ray band. Following Pe'er et al. (2007), the upper limit of Lorentz factor of the photosphere, Γ_{ph} , range between approximately 20 and 80 during the prompt phase. Considering in Pe'er's method, the plasma in the classical fireball has already reached the saturation radius, resulting in the Lorentz factor of the outflow attaining its maximum value. If the outflow were still in the acceleration phase, Γ_{ph} might be inaccurate derived from this method.

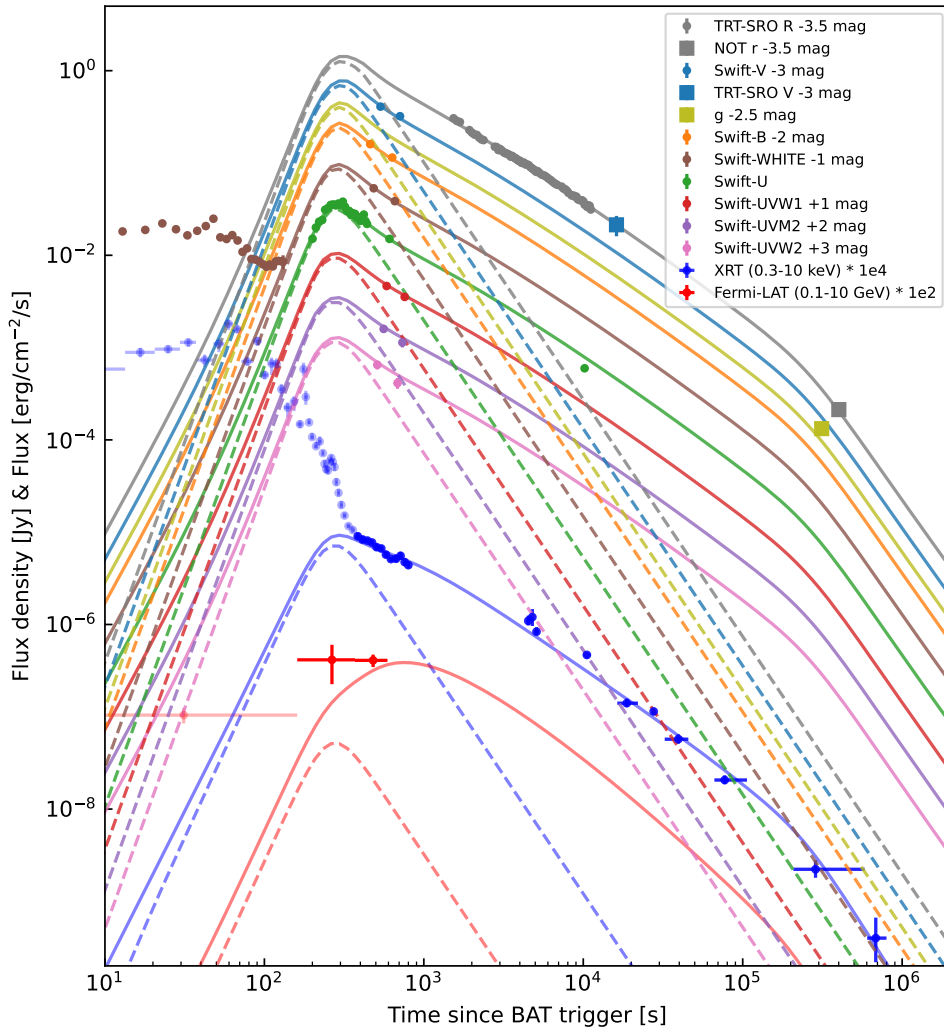


Figure 5. GRB 241030A light curves from XRT, UVOT and Fermi-LAT data. In this scenario, we consider the optical peak as dominated by RS only. Dashed line represents the RS contribution while solid line represents the sum contribution of all components.

(iii) Considering the steep rise ($\sim t^{5.3}$) observed in the U band, we adopt the scenario that both the RS and the FS considerably contribute to the afterglow at the early stage. Due to the well-sampled data of the afterglow at the early phase, some physical parameters of RS and FS can be well constrained. The best fitted model shows that the UV/optical light curves are initially dominated by the RS and the FS takes over after ~ 410 s. From RS and FS modeling, we have the initial Lorentz factor $\Gamma_0 \sim 135$, the half-opening angle $\theta_j \sim 5^\circ$ and isotropic kinetic energy $E_{k,iso} \sim 10^{56}$ erg, and $\mathcal{R}_B = (\epsilon_{B,r}/\epsilon_{B,f})^{1/2} \approx 20$. Therefore, the GRB ejecta are collimated, with a small opening angle $\sim 5^\circ$. Furthermore, the RS region is moderately magnetized, similar to what is found in the literature (Fan et al. 2002; Zhang et al. 2003), which may point towards a magnetized central engine.

In summary, with broadband and high temporal resolution observations of GRB 241030A, we find emission from the photosphere, the internal shock and the forward and reverse external shock, and their parameters are constrained.

We thank Prof. Yi-Zhong Fan for the stimulating discussion. This work is supported by the Natural Science Foundation of China (NSFC) under grant Nos. 12321003, 12225305, 12073080, the Strategic Priority Research Program of the Chinese Academy of Sciences, grant No. XDB0550400. Y.W is supported by the Jiangsu Funding Program for Excellent Postdoctoral Talent (grant No. 2024ZB110), the Postdoctoral Fellowship Program (grant No. GZC20241916) and the General Fund of the China Postdoctoral Science Foundation (grant No. 2024M763531). J. R is support by the General Fund (grant No. 2024M763530). We acknowledge the use of the public data from Swift archive, Mikulski Archive for Space Telescopes and CALSPEC. This research is based on observations under program ID TRTToO_2024005 made with the Thai Robotic Telescope, which is operated by the National Astronomical Research Institute of Thailand (Public Organization).

Facilities: Swift(BAT, XRT and UVOT), Fermi(LAT and GBM)

APPENDIX

In this appendix, we provide detailed information on the observation data and fitting results of the parameters in prompt and afterglow phases.

Table 1. *Swift* UVOT photometric observation

$T - T_0$ (s)	Exposure(s)	F_ν (Jy)	Error(Jy)	Filter
68	10	1.293×10^{-3}	2.270×10^{-4}	V
88	5	1.200×10^{-3}	8.265×10^{-5}	WHITE
93	5	1.185×10^{-3}	8.214×10^{-5}	WHITE
98	5	1.136×10^{-3}	7.939×10^{-5}	WHITE
103	5	1.045×10^{-3}	7.497×10^{-5}	WHITE
108	5	1.146×10^{-3}	8.006×10^{-5}	WHITE
113	5	1.664×10^{-3}	1.069×10^{-4}	WHITE
118	5	1.728×10^{-3}	1.103×10^{-4}	WHITE
123	5	2.032×10^{-3}	1.273×10^{-4}	WHITE
128	5	1.758×10^{-3}	1.120×10^{-4}	WHITE
133	5	1.509×10^{-3}	9.872×10^{-5}	WHITE
138	5	1.691×10^{-3}	1.084×10^{-4}	WHITE
143	5	1.902×10^{-3}	1.197×10^{-4}	WHITE
148	5	2.285×10^{-3}	1.425×10^{-4}	WHITE
153	5	1.436×10^{-3}	9.476×10^{-5}	WHITE
158	5	1.378×10^{-3}	9.184×10^{-5}	WHITE
163	5	1.518×10^{-3}	9.910×10^{-5}	WHITE
168	5	1.328×10^{-3}	8.922×10^{-5}	WHITE
173	5	9.998×10^{-4}	7.276×10^{-5}	WHITE
178	5	1.091×10^{-3}	7.730×10^{-5}	WHITE
183	5	8.365×10^{-4}	6.469×10^{-5}	WHITE
188	5	8.245×10^{-4}	6.395×10^{-5}	WHITE
193	5	7.855×10^{-4}	6.186×10^{-5}	WHITE
198	5	7.329×10^{-4}	5.940×10^{-5}	WHITE
203	5	6.894×10^{-4}	5.724×10^{-5}	WHITE
208	5	7.281×10^{-4}	5.911×10^{-5}	WHITE
213	5	6.951×10^{-4}	5.763×10^{-5}	WHITE
218	5	7.865×10^{-4}	6.187×10^{-5}	WHITE
223	5	7.976×10^{-4}	6.245×10^{-5}	WHITE
228	5	7.905×10^{-4}	6.211×10^{-5}	WHITE
300	10	5.044×10^{-3}	2.700×10^{-4}	U
310	10	6.677×10^{-3}	3.344×10^{-4}	U
320	10	7.704×10^{-3}	3.751×10^{-4}	U
330	10	8.042×10^{-3}	3.894×10^{-4}	U
340	10	1.040×10^{-2}	4.886×10^{-4}	U
350	10	1.083×10^{-2}	5.071×10^{-4}	U
360	10	1.172×10^{-2}	5.473×10^{-4}	U
370	10	1.186×10^{-2}	5.541×10^{-4}	U
380	10	1.158×10^{-2}	5.410×10^{-4}	U
390	10	1.212×10^{-2}	5.660×10^{-4}	U
400	10	1.171×10^{-2}	5.470×10^{-4}	U

$T - T_0(s)$	Exposure(s)	$F_\nu(\text{Jy})$	Error(Jy)	Filter
410	10	1.271×10^{-2}	5.936×10^{-4}	U
420	10	1.119×10^{-2}	5.236×10^{-4}	U
430	10	1.008×10^{-2}	4.747×10^{-4}	U
440	10	1.008×10^{-2}	4.748×10^{-4}	U
450	10	9.084×10^{-3}	4.319×10^{-4}	U
460	10	9.505×10^{-3}	4.500×10^{-4}	U
470	10	9.350×10^{-3}	4.436×10^{-4}	U
480	10	8.519×10^{-3}	4.086×10^{-4}	U
490	10	8.615×10^{-3}	4.127×10^{-4}	U
500	10	7.875×10^{-3}	3.823×10^{-4}	U
510	10	8.314×10^{-3}	4.003×10^{-4}	U
520	10	9.211×10^{-3}	4.376×10^{-4}	U
530	10	7.840×10^{-3}	3.810×10^{-4}	U
540	9	7.299×10^{-3}	3.749×10^{-4}	U
561	19	1.053×10^{-2}	3.889×10^{-4}	B
585	19	4.882×10^{-3}	2.048×10^{-4}	WHITE
611	19	5.769×10^{-4}	6.199×10^{-5}	UVW2
635	19	1.176×10^{-2}	5.618×10^{-4}	V
660	18	1.159×10^{-3}	1.115×10^{-4}	UVM2
684	18	2.092×10^{-3}	1.333×10^{-4}	UVW1
709	19	5.024×10^{-3}	2.089×10^{-4}	U
734	19	7.542×10^{-3}	2.980×10^{-4}	B
758	19	3.540×10^{-3}	1.308×10^{-4}	WHITE
784	19	3.665×10^{-4}	4.896×10^{-5}	UVW2
804	19	9.264×10^{-3}	4.788×10^{-4}	V
834	17	8.260×10^{-4}	9.506×10^{-5}	UVM2
858	18	1.593×10^{-3}	1.140×10^{-4}	UVW1
10294	300	1.991×10^{-4}	9.556×10^{-6}	U

End of the Table

Note. The photometry results presented in this table have not been corrected for Galactic extinction.

Table 2. Ground-base photometric observation

$T_{mid} - T_0$ (s)	Exposure(s)	Filter	Mag (AB)	Error(AB)	Ins.
1636	60	R	14.77	0.01	TRT-SRO
1710	60	R	14.84	0.01	TRT-SRO
1783	60	R	14.87	0.01	TRT-SRO
2031	60	R	15.09	0.01	TRT-SRO
2105	60	R	15.16	0.01	TRT-SRO
2177	60	R	15.21	0.01	TRT-SRO
2250	60	R	15.22	0.01	TRT-SRO
2322	60	R	15.29	0.01	TRT-SRO
2395	60	R	15.34	0.01	TRT-SRO
2468	60	R	15.36	0.01	TRT-SRO
2889	60	R	15.54	0.01	TRT-SRO
2962	60	R	15.55	0.01	TRT-SRO
3034	60	R	15.63	0.01	TRT-SRO
3106	60	R	15.6	0.01	TRT-SRO
3177	60	R	15.64	0.01	TRT-SRO
3250	60	R	15.68	0.01	TRT-SRO
3321	60	R	15.71	0.01	TRT-SRO
3394	60	R	15.72	0.01	TRT-SRO
3467	60	R	15.74	0.01	TRT-SRO
3538	60	R	15.76	0.01	TRT-SRO
3610	60	R	15.81	0.01	TRT-SRO
3682	60	R	15.79	0.01	TRT-SRO
3753	60	R	15.82	0.01	TRT-SRO
3825	60	R	15.85	0.01	TRT-SRO
3897	60	R	15.86	0.01	TRT-SRO
3968	60	R	15.9	0.01	TRT-SRO
4040	60	R	15.92	0.01	TRT-SRO
41125	60	R	15.92	0.01	TRT-SRO
4185	60	R	15.97	0.01	TRT-SRO
4257	60	R	15.98	0.01	TRT-SRO
4344	90	R	15.97	0.01	TRT-SRO
4447	90	R	16.02	0.01	TRT-SRO
4550	90	R	16.02	0.01	TRT-SRO
4652	90	R	16.04	0.01	TRT-SRO
4755	90	R	16.09	0.01	TRT-SRO
4857	90	R	16.12	0.01	TRT-SRO
4958	90	R	16.15	0.01	TRT-SRO
5061	90	R	16.18	0.01	TRT-SRO
5162	90	R	16.22	0.01	TRT-SRO
5265	90	R	16.2	0.01	TRT-SRO
5413	180	R	16.25	0.01	TRT-SRO
5606	180	R	16.3	0.01	TRT-SRO
5798	180	R	16.32	0.01	TRT-SRO
5990	180	R	16.36	0.01	TRT-SRO
6182	180	R	16.41	0.01	TRT-SRO
6375	180	R	16.45	0.01	TRT-SRO
6567	180	R	16.5	0.01	TRT-SRO

$T_{mid} - T_0(s)$	Exposure(s)	Filter	Mag (AB)	Error	Ins.
6758	180	R	16.54	0.01	TRT-SRO
6951	180	R	16.57	0.01	TRT-SRO
7410	180	R	16.62	0.01	TRT-SRO
7601	180	R	16.67	0.01	TRT-SRO
7793	180	R	16.69	0.01	TRT-SRO
7986	180	R	16.73	0.01	TRT-SRO
8179	180	R	16.79	0.01	TRT-SRO
8565	180	R	16.86	0.01	TRT-SRO
8758	180	R	16.86	0.01	TRT-SRO
8950	180	R	16.89	0.01	TRT-SRO
9143	180	R	16.89	0.02	TRT-SRO
9336	180	R	16.96	0.02	TRT-SRO
9528	180	R	16.98	0.02	TRT-SRO
9721	180	R	16.99	0.02	TRT-SRO
9914	180	R	16.99	0.02	TRT-SRO
10106	180	R	17.02	0.03	TRT-SRO
10299	180	R	17.11	0.03	TRT-SRO
10491	180	R	17.11	0.04	TRT-SRO
10682	180	R	17.17	0.04	TRT-SRO
10874	180	R	17.13	0.04	TRT-SRO
11067	180	R	17.14	0.04	TRT-SRO
11254	180	R	17.24	0.04	TRT-SRO
15767	3x150	B	> 18.1		TRT-SRO
16254	3x150	V	18.14	0.27	TRT-SRO
16953	3x150	R	> 17.6		TRT-SRO
17442	3x150	I	> 15.7		TRT-SRO
312924	3x300	g	23.08	0.13	NOT
314248	5x300	z	> 21.8		NOT
400777	3x600	r	23.17	0.12	NOT

End of the Table

Note. The photometry results presented in this table have not been corrected for Galactic extinction.

Data	Model	start [s]	stop [s]	α	E_{peak} [keV]	norm	kT [keV]	norm _{BB}	Δ_{BIC}
XRT+BAT+GBM	PL+BB	85	90	$-1.45^{+0.03}_{-0.03}$		$1.33^{+0.15}_{-0.15}$	$2.58^{+0.18}_{-0.18}$	$0.26^{+0.04}_{-0.04}$	31.06
XRT+BAT	PL+BB	90	95	$-1.77^{+0.07}_{-0.07}$		$1.78^{+0.35}_{-0.37}$	$1.40^{+0.39}_{-0.24}$	$0.18^{+0.07}_{-0.04}$	36.48
XRT+BAT	PL+BB	95	100	$-1.70^{+0.16}_{-0.13}$		$0.75^{+0.33}_{-0.32}$	$0.79^{+0.08}_{-0.06}$	$0.10^{+0.02}_{-0.02}$	36.47
XRT+BAT	PL+BB	100	105	$-1.71^{+0.14}_{-0.11}$		$0.87^{+0.34}_{-0.34}$	$0.82^{+0.09}_{-0.07}$	$0.11^{+0.02}_{-0.02}$	38.11
XRT+BAT+GBM	CPL+BB	105	110	$-1.24^{+0.06}_{-0.05}$	$74.63^{+20.48}_{-14.10}$	$2.22^{+0.27}_{-0.29}$	$1.87^{+0.30}_{-0.35}$	$0.25^{+0.06}_{-0.06}$	22.56
XRT+BAT+GBM	CPL+BB	110	115	$-1.02^{+0.03}_{-0.03}$	$248.38^{+36.77}_{-30.46}$	$2.38^{+0.20}_{-0.20}$	$3.06^{+0.27}_{-0.22}$	$0.59^{+0.07}_{-0.07}$	62.80
XRT+BAT+GBM	CPL+BB	115	120	$-1.18^{+0.03}_{-0.03}$	$129.83^{+12.18}_{-10.63}$	$2.49^{+0.21}_{-0.21}$	$2.17^{+0.16}_{-0.16}$	$0.47^{+0.06}_{-0.06}$	66.47
XRT+BAT+GBM	CPL+BB	120	125	$-1.08^{+0.03}_{-0.03}$	$193.98^{+26.72}_{-22.43}$	$3.01^{+0.26}_{-0.26}$	$2.63^{+0.16}_{-0.15}$	$0.84^{+0.08}_{-0.08}$	105.36
XRT+BAT+GBM	CPL+BB	125	130	$-1.24^{+0.05}_{-0.04}$	$63.53^{+11.21}_{-8.74}$	$3.39^{+0.37}_{-0.37}$	$1.67^{+0.18}_{-0.18}$	$0.45^{+0.07}_{-0.07}$	56.06
XRT+BAT+GBM	CPL+BB	130	135	$-1.16^{+0.02}_{-0.02}$	$158.16^{+19.18}_{-16.13}$	$5.17^{+0.36}_{-0.36}$	$3.28^{+0.32}_{-0.27}$	$0.58^{+0.09}_{-0.08}$	42.99
XRT+BAT+GBM	CPL+BB	135	140	$-1.15^{+0.02}_{-0.02}$	$402.90^{+78.04}_{-60.35}$	$4.22^{+0.29}_{-0.30}$	$3.01^{+0.80}_{-0.59}$	$0.35^{+0.08}_{-0.09}$	11.80
XRT+BAT+GBM	CPL+BB	140	145	$-1.17^{+0.02}_{-0.02}$	$431.21^{+86.15}_{-66.43}$	$3.90^{+0.30}_{-0.30}$	$2.33^{+0.35}_{-0.34}$	$0.25^{+0.07}_{-0.07}$	2.97
XRT+BAT+GBM	CPL+BB	145	150	$-0.82^{+0.04}_{-0.04}$	$150.49^{+11.80}_{-10.86}$	$2.19^{+0.26}_{-0.25}$	$1.45^{+0.15}_{-0.14}$	$0.29^{+0.06}_{-0.06}$	17.91
XRT+BAT+GBM	CPL+BB	150	155	$-1.19^{+0.04}_{-0.04}$	$63.06^{+8.57}_{-6.94}$	$3.90^{+0.34}_{-0.34}$	$2.77^{+0.16}_{-0.15}$	$0.73^{+0.08}_{-0.08}$	76.81
XRT+BAT+GBM	CPL+BB	155	160	$-1.34^{+0.04}_{-0.04}$	$80.01^{+18.38}_{-12.99}$	$5.70^{+0.49}_{-0.49}$	$2.41^{+0.16}_{-0.15}$	$0.99^{+0.09}_{-0.09}$	112.17
XRT+BAT+GBM	CPL+BB	160	165	$-1.05^{+0.03}_{-0.03}$	$139.80^{+10.52}_{-9.50}$	$5.96^{+0.48}_{-0.47}$	$2.13^{+0.23}_{-0.19}$	$0.68^{+0.11}_{-0.11}$	26.42
XRT+BAT+GBM	CPL+BB	165	170	$-1.10^{+0.04}_{-0.03}$	$78.20^{+6.10}_{-5.44}$	$5.69^{+0.55}_{-0.54}$	$2.00^{+0.28}_{-0.24}$	$0.56^{+0.11}_{-0.11}$	17.93
XRT+BAT+GBM	CPL+BB	170	175	$-1.25^{+0.10}_{-0.08}$	$36.47^{+6.56}_{-5.34}$	$3.11^{+0.64}_{-0.66}$	$1.08^{+0.11}_{-0.09}$	$0.46^{+0.06}_{-0.05}$	71.43
XRT+BAT	PL+BB	175	180	$-1.98^{+0.07}_{-0.07}$		$3.66^{+0.70}_{-0.73}$	$1.04^{+0.15}_{-0.11}$	$0.33^{+0.04}_{-0.04}$	73.46
XRT+BAT	CPL+BB	180	185	$-1.63^{+0.09}_{-0.08}$	$23.30^{+14.21}_{-7.26}$	$4.35^{+0.61}_{-0.66}$	$1.10^{+0.28}_{-0.18}$	$0.19^{+0.04}_{-0.04}$	13.93
XRT+BAT+GBM	CPL+BB	185	190	$-1.33^{+0.03}_{-0.03}$	$96.20^{+16.21}_{-12.80}$	$6.31^{+0.52}_{-0.52}$	$2.15^{+0.22}_{-0.20}$	$0.56^{+0.09}_{-0.09}$	30.63
XRT+BAT+GBM	CPL+BB	190	195	$-1.33^{+0.10}_{-0.09}$	$17.00^{+4.07}_{-3.09}$	$4.02^{+0.57}_{-0.61}$	$1.24^{+0.14}_{-0.13}$	$0.46^{+0.07}_{-0.06}$	47.52
XRT+BAT	PL+BB	195	200	$-1.82^{+0.10}_{-0.09}$		$2.08^{+0.65}_{-0.64}$	$0.79^{+0.06}_{-0.05}$	$0.34^{+0.03}_{-0.03}$	112.81
XRT+BAT	PL+BB	200	205	$-2.26^{+0.15}_{-0.21}$		$2.33^{+0.61}_{-0.64}$	$0.73^{+0.09}_{-0.07}$	$0.19^{+0.03}_{-0.02}$	49.68
XRT+BAT	PL+BB	205	210	$-1.78^{+0.05}_{-0.05}$		$3.75^{+0.60}_{-0.62}$	$0.98^{+0.19}_{-0.13}$	$0.18^{+0.03}_{-0.03}$	25.36
XRT+BAT	PL+BB	210	215	$-1.94^{+0.05}_{-0.05}$		$4.77^{+0.65}_{-0.66}$	$1.04^{+0.11}_{-0.09}$	$0.36^{+0.04}_{-0.04}$	82.08
XRT+BAT	CPL+BB	215	220	$-1.60^{+0.06}_{-0.06}$	$47.27^{+26.15}_{-13.17}$	$5.05^{+0.62}_{-0.65}$	$1.26^{+0.23}_{-0.17}$	$0.30^{+0.06}_{-0.05}$	29.94
XRT+BAT	PL+BB	220	225	$-1.86^{+0.04}_{-0.04}$		$5.11^{+0.61}_{-0.63}$	$1.13^{+0.22}_{-0.15}$	$0.28^{+0.05}_{-0.04}$	52.32
XRT+BAT	PL+BB	225	230	$-1.98^{+0.06}_{-0.06}$		$3.05^{+0.45}_{-0.47}$	$0.84^{+0.12}_{-0.09}$	$0.14^{+0.02}_{-0.02}$	38.05

Table 3. Best spectral fit result from XRT, BAT, and GBM. Joint fit obtained using either with the PL+BB or CPL+BB model. Spectral normalizations are computed in $\text{ph} \cdot \text{cm}^{-2} \cdot \text{s}^{-1}$ at 1keV. Here, α is the photon index of PL or CPL, Δ_{BIC} is differences of BIC value between model with BB and model without BB. Except for the epoch at 140 - 145 seconds, where $\Delta_{BIC} = 2.97$, we find $\Delta_{BIC} > 10$ in all other epochs and $\Delta_{BIC} > 30$ in 20 of 29 epochs, which is a strong evidence of an additional thermal component.

Table 4. SED Data at $T_0 + 755\text{s}$

Filter	F_ν (Jy)	Error(Jy)
WHITE	3.540×10^{-3}	1.308×10^{-4}
V	1.020×10^{-2}	5.274×10^{-4}
U	4.602×10^{-3}	1.913×10^{-4}
B	7.250×10^{-3}	2.865×10^{-4}
UVW1	1.822×10^{-3}	1.162×10^{-4}
UVW2	4.291×10^{-4}	4.611×10^{-5}
UVM2	9.604×10^{-4}	9.240×10^{-5}

Table 5. Fitting results of model parameters

Parameter	Prior range	Posterior value
$\log_{10} \Gamma_0$	[1, 2.5]	$2.13^{+0.04}_{-0.04}$
$\log_{10} \epsilon_{e,f}$	[-3, -0.1]	$-1.87^{+0.06}_{-0.05}$
$\log_{10} \epsilon_{B,f}$	[-7, -0.1]	$-5.74^{+0.07}_{-0.07}$
$\log_{10} \theta_j$ (rad)	[-2, 0]	$-1.10^{+0.04}_{-0.04}$
$\log_{10} E_{k,iso}$ (erg)	[51, 56]	$55.83^{+0.09}_{-0.09}$
pf	[2, 3]	$2.77^{+0.01}_{-0.01}$
$\log_{10} \epsilon_{e,r}$	[-3, -0.1]	$-3.15^{+0.09}_{-0.09}$
$\log_{10} \epsilon_{B,r}$	[-7, -0.1]	$-3.19^{+0.02}_{-0.01}$
p_r	[2, 3]	$2.09^{+0.05}_{-0.03}$
$\log_{10} n_0$	[-3, 3]	$1.35^{+0.26}_{-0.25}$
$\log_{10} f_{sys}$	[-2, 0]	$-1.58^{+0.05}_{-0.04}$

^aUniform prior distribution.

^bThe confidence interval is set to 1σ .

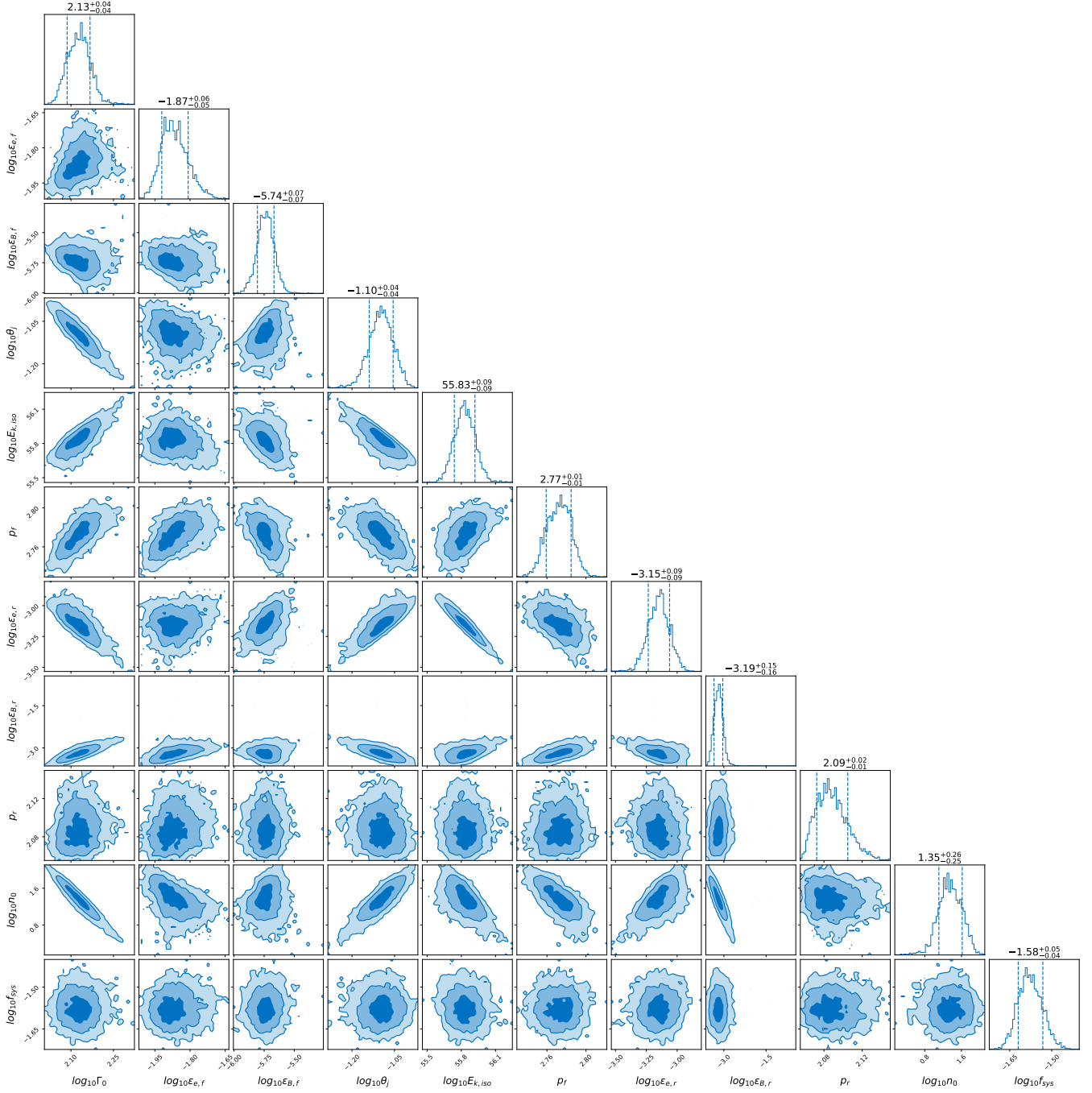


Figure 6. Constrained parameters of the afterglow model for GRB 241030A. Here Γ_0 is the initial Lorentz factor, ϵ_e is fraction of energy of relativistic electrons, ϵ_b is fraction of the energy of magnetic field, θ_j is the half-opening angle in radians, $E_{k,iso}$ is the isotropic kinetic energy, p is the electron energy distribution index, n_0 is the medium number density. And the additional subscripts f and r represent the FS and RS, respectively.

REFERENCES

- Akerlof, C., Balsano, R., Barthelmy, S., et al. 1999, *Nature*, 398, 400, doi: [10.1038/18837](https://doi.org/10.1038/18837)
- Ambrosi, E., Williams, M. A., Dichiara, S., et al. 2024, GRB Coordinates Network, 37988, 1
- Atwood, W. B., Abdo, A. A., Ackermann, M., et al. 2009, *ApJ*, 697, 1071, doi: [10.1088/0004-637X/697/2/1071](https://doi.org/10.1088/0004-637X/697/2/1071)
- Ballet, J., Bruel, P., Burnett, T. H., Lott, B., & The Fermi-LAT collaboration. 2023, arXiv e-prints, arXiv:2307.12546, doi: [10.48550/arXiv.2307.12546](https://doi.org/10.48550/arXiv.2307.12546)
- Barthelmy, S. D., Barbier, L. M., Cummings, J. R., et al. 2005, *Space Science Reviews*, 120, 143, doi: [10.1007/s11214-005-5096-3](https://doi.org/10.1007/s11214-005-5096-3)
- Beardmore, A. P., Evans, P. A., Goad, M. R., Osborne, J. P., & Swift-XRT Team. 2024, GRB Coordinates Network, 37962, 1
- Breeveld, A. A., Klingler, N. J., & Swift/UVOT Team. 2024, GRB Coordinates Network, 37974, 1
- Buchner, J., Georgakakis, A., Nandra, K., et al. 2014, *A&A*, 564, A125, doi: [10.1051/0004-6361/201322971](https://doi.org/10.1051/0004-6361/201322971)
- Bukhari, S. A. M., Sajjad, S., & Murtaza, U. 2022, *Advances in Space Research*, 70, 1512, doi: [10.1016/j.asr.2022.05.073](https://doi.org/10.1016/j.asr.2022.05.073)
- Burrows, D. N., Hill, J. E., Nousek, J. A., et al. 2005, *Space Science Reviews*, 120, 165, doi: [10.1007/s11214-005-5097-2](https://doi.org/10.1007/s11214-005-5097-2)
- Evans, P. A., Beardmore, A. P., Page, K. L., et al. 2007, *A&A*, 469, 379, doi: [10.1051/0004-6361:20077530](https://doi.org/10.1051/0004-6361:20077530)
- Evans, P. A., Beardmore, A. P., Page, K. L., et al. 2009, *Monthly Notices of the Royal Astronomical Society*, 397, 1177, doi: [10.1111/j.1365-2966.2009.14913.x](https://doi.org/10.1111/j.1365-2966.2009.14913.x)
- Fan, Y.-Z., Dai, Z.-G., Huang, Y.-F., & Lu, T. 2002, *ChJA&A*, 2, 449, doi: [10.1088/1009-9271/2/5/449](https://doi.org/10.1088/1009-9271/2/5/449)
- Fan, Y. Z., Wei, D. M., & Wang, C. F. 2004, *A&A*, 424, 477, doi: [10.1051/0004-6361:20041115](https://doi.org/10.1051/0004-6361:20041115)
- Fermi GBM Team. 2024, GRB Coordinates Network, 37955, 1
- Fitzpatrick, E. L. 1999, *PASP*, 111, 63, doi: [10.1086/316293](https://doi.org/10.1086/316293)
- Flewelling, H. A., Magnier, E. A., Chambers, K. C., et al. 2020, *The Astrophysical Journal Supplement Series*, 251, 7, doi: [10.3847/1538-4365/abb82d](https://doi.org/10.3847/1538-4365/abb82d)
- Gehrels, N., Chincarini, G., Giommi, P., et al. 2004, *The Astrophysical Journal*, 611, 1005, doi: [10.1086/422091](https://doi.org/10.1086/422091)
- Godet, O., Nasser, G., Atteia, J. ., et al. 2014, in *Society of Photo-Optical Instrumentation Engineers (SPIE) Conference Series*, Vol. 9144, *Space Telescopes and Instrumentation 2014: Ultraviolet to Gamma Ray*, ed. T. Takahashi, J.-W. A. den Herder, & M. Bautz, 914424, doi: [10.1117/12.2055507](https://doi.org/10.1117/12.2055507)
- Goldstein, A., Cleveland, W. H., & Kocevski, D. 2022, Fermi GBM Data Tools: v1.1.1. <https://fermi.gsfc.nasa.gov/ssc/data/analysis/gbm>
- Huang, L.-Y., Wang, X.-G., Zheng, W., et al. 2018, *ApJ*, 859, 163, doi: [10.3847/1538-4357/aaba6e](https://doi.org/10.3847/1538-4357/aaba6e)
- Jin, Z.-P., Zhou, H., Wang, Y., et al. 2023, *Nature Astronomy*, 7, 1108, doi: [10.1038/s41550-023-02005-w](https://doi.org/10.1038/s41550-023-02005-w)
- Klingler, N. J., Dichiara, S., Gupta, R., et al. 2024, GRB Coordinates Network, 37956, 1
- Lang, D., Hogg, D. W., Mierle, K., Blanton, M., & Roweis, S. 2010, *The Astronomical Journal*, 139, 1782, doi: [10.1088/0004-6256/139/5/1782](https://doi.org/10.1088/0004-6256/139/5/1782)
- Li, L., Liang, E.-W., Tang, Q.-W., et al. 2012, *ApJ*, 758, 27, doi: [10.1088/0004-637X/758/1/27](https://doi.org/10.1088/0004-637X/758/1/27)
- Liang, E.-W., Zhang, B.-B., & Zhang, B. 2007, *ApJ*, 670, 565, doi: [10.1086/521870](https://doi.org/10.1086/521870)
- Meegan, C., Lichti, G., Bhat, P. N., et al. 2009, *ApJ*, 702, 791, doi: [10.1088/0004-637X/702/1/791](https://doi.org/10.1088/0004-637X/702/1/791)
- Mészáros, P., & Rees, M. J. 1997, *The Astrophysical Journal*, 476, 232, doi: [10.1086/303625](https://doi.org/10.1086/303625)
- . 1999, *Monthly Notices of the Royal Astronomical Society*, 306, L39, doi: [10.1046/j.1365-8711.1999.02800.x](https://doi.org/10.1046/j.1365-8711.1999.02800.x)
- Pe'er, A., Ryde, F., Wijers, R. A. M. J., Mészáros, P., & Rees, M. J. 2007, *The Astrophysical Journal*, 664, L1, doi: [10.1086/520534](https://doi.org/10.1086/520534)
- Pillera, R., Gupta, R., Kocevski, D., Loizzo, P., & Fermi-LAT Collaboration. 2024, GRB Coordinates Network, 37979, 1
- Planck Collaboration, Aghanim, N., Akrami, Y., et al. 2020, *A&A*, 641, A6, doi: [10.1051/0004-6361/201833910](https://doi.org/10.1051/0004-6361/201833910)
- Ren, J., Wang, Y., & Dai, Z.-G. 2024, *ApJ*, 962, 115, doi: [10.3847/1538-4357/ad1bcd](https://doi.org/10.3847/1538-4357/ad1bcd)
- Romano, P., Campana, S., Chincarini, G., et al. 2006, *A&A*, 456, 917, doi: [10.1051/0004-6361:20065071](https://doi.org/10.1051/0004-6361:20065071)
- Roming, P. W. A., Kennedy, T. E., Mason, K. O., et al. 2005, *Space Sci Rev*, 120, 95, doi: [10.1007/s11214-005-5095-4](https://doi.org/10.1007/s11214-005-5095-4)
- Sari, R., & Piran, T. 1999, *The Astrophysical Journal*, 517, L109, doi: [10.1086/312039](https://doi.org/10.1086/312039)
- SVOM/C-GFT Team, WU, C., Kang, Z., et al. 2024, GRB Coordinates Network, 37970, 1
- SVOM/GRM Team, Wang, Y., Wang, C.-W., et al. 2024, GRB Coordinates Network, 37972, 1
- SVOM/VT commissioning Team, Qiu, Y. L., Li, H. L., et al. 2024, GRB Coordinates Network, 37965, 1
- Tody, D. 1986, 627, 733, doi: [10.1117/12.968154](https://doi.org/10.1117/12.968154)
- Wang, J., Xin, L. P., Qiu, Y. L., et al. 2024, *Research in Astronomy and Astrophysics*, 24, 115006, doi: [10.1088/1674-4527/ad7fb5](https://doi.org/10.1088/1674-4527/ad7fb5)

- Wang, X.-G., Zhang, B., Liang, E.-W., et al. 2015, *ApJS*, 219, 9, doi: [10.1088/0067-0049/219/1/9](https://doi.org/10.1088/0067-0049/219/1/9)
- Wang, Y., Xia, Z.-Q., Zheng, T.-C., Ren, J., & Fan, Y.-Z. 2023, *The Astrophysical Journal Letters*, 953, L8, doi: [10.3847/2041-8213/ace7d4](https://doi.org/10.3847/2041-8213/ace7d4)
- Wei, D. 2007, *MNRAS*, 374, 525, doi: [10.1111/j.1365-2966.2006.11156.x](https://doi.org/10.1111/j.1365-2966.2006.11156.x)
- Wei, J., & Cordier, B. 2024, *Space-Based Multi-band Astronomical Variable Objects Monitor (SVOM)*, ed. C. Bambi & A. Santangelo (Singapore: Springer Nature Singapore), 1409–1421, doi: [10.1007/978-981-19-6960-7_154](https://doi.org/10.1007/978-981-19-6960-7_154)
- Wilms, J., Allen, A., & McCray, R. 2000, *ApJ*, 542, 914, doi: [10.1086/317016](https://doi.org/10.1086/317016)
- Yi, S.-X., Wu, X.-F., & Dai, Z.-G. 2013, *ApJ*, 776, 120, doi: [10.1088/0004-637X/776/2/120](https://doi.org/10.1088/0004-637X/776/2/120)
- Zhang, B., & Kobayashi, S. 2005, *ApJ*, 628, 315, doi: [10.1086/429787](https://doi.org/10.1086/429787)
- Zhang, B., Kobayashi, S., & Mészáros, P. 2003, *ApJ*, 595, 950, doi: [10.1086/377363](https://doi.org/10.1086/377363)
- Zheng, W., Brink, T. G., Filippenko, A. V., Yang, Y., & KAIT GRB Team. 2024, *GRB Coordinates Network*, 37959, 1
- Zhou, H., Jin, Z.-P., Covino, S., Fan, Y.-Z., & Wei, D.-M. 2023, *ApJS*, 268, 65, doi: [10.3847/1538-4365/acf20a](https://doi.org/10.3847/1538-4365/acf20a)